Faraday Discuss., 1996, **104**, 65–78

Use of complementary neutron scattering techniques in studying the effect of a solid/liquid interface on bulk solution structures†

Paul D. Butler,*[a] William A. Hamilton,[a] Linda J. Magid,[b] John B. Hayter,[b] Tania M. Slawecki[c] and Boualem Hammouda[c]

[a] *Oak Ridge National Laboratory, PO Box 2008, Oak Ridge, TN 37831-6393, USA*
[b] *Chemistry Department, University of Tennessee, Knoxville, TN 37996-1600, USA*
[c] *National Institute of Science and Technology, Gaithersburg, MD 20899, USA*

By appropriate combination of neutron scattering techniques, it is possible to obtain structural information at various depths from a solid/liquid interface and thus probe in some detail how the surface structures evolve into bulk structures. We have used neutron reflectometry (NR) with a newly developed shear cell, near-surface small-angle neutron scattering (NSSANS) again in combination with the new shear cell, and regular small-angle neutron scattering (SANS) with a standard Couette shear cell to probe the structures formed in our aqueous surfactant systems and how they react to a flow field, particularly in the near-surface region of a solid/liquid interface. We present data for a 20×10^{-3} M aqueous solution of 70% cetyltrimethylammonium 3,5-dichlorobenzoate (CTA3,5ClBz) and 30% CTAB. This system forms a very viscoelastic solution containing long thread-like micelles. NR only probes to a depth of *ca.* 0.5 μm from the surface in these systems and clearly indicates that adsorbed onto the surface is a surfactant layer which is insensitive to shear. The depth probed by the NSSANS is of the order of 20–30 μm and is determined by the transmission of the sample, the angle of incidence and the wavelength. In this region, the rods align under shear into a remarkably well ordered hexagonal crystal. The SANS from the Couette cell averages over the entire sample, so that the signal is dominated by scattering from the bulk. While the near-surface hexagonal structure is clearly visible, these data are not consistent with the crystal structure persisting throughout the bulk, leading to the postulate that the bulk structure is a 2D liquid where the rods align with the flow, but do not order in the other two dimensions.

CTAB is probably the most studied cationic surfactant. An aqueous solution of CTAB contains relatively small spherical micelles.[1] Upon addition of supporting electrolyte (*e.g.* NaBr), the micelles elongate into rod-like structures, also known as Debye micelles after Peter Debye who first suggested the rod-like micellar shape for these CTAB systems in 1951.[2] At high salt and surfactant concentrations, the solutions become extremely viscous as the rods become long enough (and concentrated enough) to overlap,[3] which, in analogy to polymer solutions, is usually referred to as the semi-dilute regime. In the late 1960s to early 1970s it was discovered that addition of certain substituted aromatic salts drastically altered the rheological properties of CTAB solutions.[4–6] Not only did they become quite viscous at very low concentrations, but they also exhibited elastic characteristics or viscoelastic behaviour. In 1976 Gravsholt[7] showed that simply replacing the bromide counterion with one of the appropriate aromatic ions produced the same effect, with no added salt of any kind. This effect is very sensitive not

† This work was performed at the High Flux Isotope Reactor at Oak Ridge National Laboratory and on the NG3 SANS instrument at the National Institute of Science and Technology (NIST).

only to the nature of the substituent on the aromatic ring but also its position, with the *o*-hydroxybenzoate, and the *p*- and *m*-chlorobenzoate producing the effect while the *p*- and *m*-hydroxy and the *o*-chlorobenzoate do not. In 1986, Carver[8] showed that the effect was even more pronounced for the disubstituted chlorobenzoates (*e.g.* 3,5-dichlorobenzoate or 3,5ClBz). Thus the zero shear viscosity for example of a 20×10^{-3} M (1% by weight) aqueous solution of CTA3,5ClBz is 1200 Pa s, while the same concentration of a solution of CTA2,6ClBz is 0.0011 Pa s,[9] close to that of water at 0.001 02 Pa s.

Recently, we have begun investigating systems of mixed surfactant (CTAB and CTA3,5ClBz). Even with 40% CTAB the system is still viscoelastic, at least at concentrations of 10×10^{-3} M and above. The primary effect of small amounts of CTAB seems to be to increase the surface charge density on the micelles, thereby making them stiffer and affecting the kinetics of alignment and decay of alignment of the rods in the bulk under shear.[10] Here, we discuss structural aspects of a 20×10^{-3} M solution of the mixed counterion system 70% 3,5ClBz and 30% Br^- made by making the solution 14×10^{-3} M in CTA3,5ClBz and 6×10^{-3} M in CTAB (70/30 CTA3,5ClBz/Br).

One of the main interests in surfactants which form viscoelastic solutions at low concentrations is in their drag reduction and lubricating properties. Clearly, the microscopic behaviour which generates such macroscopic effects must take place near the surface of the fluid under flow. In this paper we characterize the micellar structures and orientations under flow near a quartz surface.

The first tool used in our investigation of structural effects at the solid/liquid interface was neutron reflectometry (NR). Neutrons were chosen both because of their penetrating power (allowing the beam to travel a substantial distance in the solid before reaching the interface) and because of the large contrast obtainable between the particles and the solvent (by using D_2O as the solvent for the protonated surfactant). This technique has been used successfully to study polymer thin films[11,12] and structures of surfactant layers at the air/water interface,[13,14] for example. Reflectivity, however, only measures changes in the scattering length density (β) in the direction normal to the interface ($d\beta/dz$) and, in our case, perpendicular to the flow direction and parallel to the shear gradient. Near-surface small-angle neutron scattering (NSSANS), and bulk Couette SANS were therefore used to obtain a more complete, 3D picture of the structures formed near the interface, and to look at how they change as a function of distance from the surface.

Experimental

Reflectometry

NR was performed on the MIRROR instrument at the High Flux Isotope Reactor (HFIR) at the Oak Ridge National Laboratory.[15,16] A pyrolytic graphite monochromator provides an intense incident beam at a wavelength of 0.259 nm. The linear position-sensitive detector tracks the specular and off-specular scattering in a horizontal plane with an instrumental resolution ΔQ of 0.01 nm^{-1}. Each 2D data set consists of a stacked series of 1D position-sensitive detector (PSD) images (horizontal axis) of the scattering normal to the reflection plane (Q_z) as the incident angle is increased (vertical axis) made as the detector tracks the reflected beam in a $\theta : 2\theta$ scan. Q is expressed in the familiar form $4\pi \sin \theta/\lambda$ with the difference that θ is defined here as the angle of incidence onto the reflecting surface rather than the usual scattering definition of half the angle between the direct beam and the detection direction; λ is of course the wavelength. When necessary to distinguish between this Q and the Q from scattering, this Q will be written as Q_R while the scattering Q will be written as Q_s or identified by its direction in space (Q_x, Q_y, Q_z). In reflectometry, the z direction is always referenced as the normal to

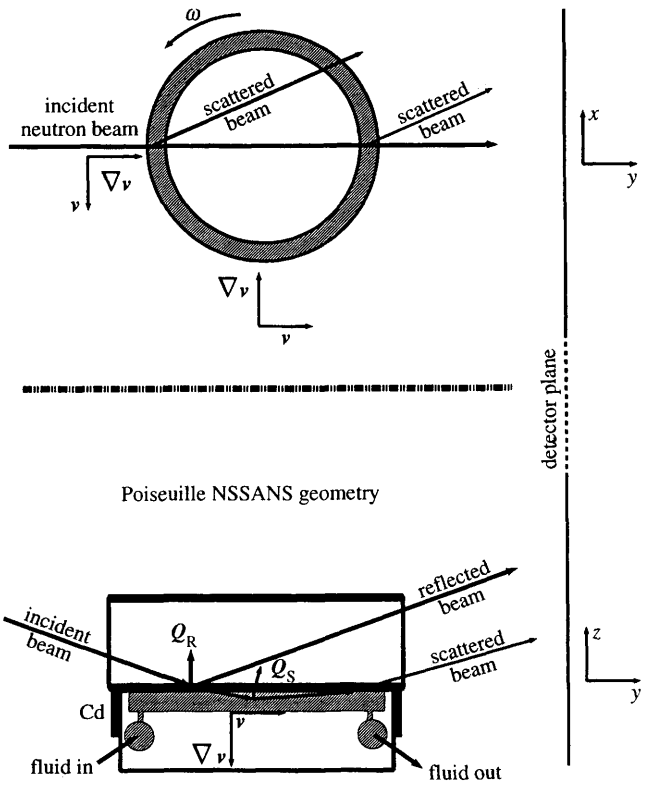

Fig. 1 Geometry of the SANS and NSSANS experiments. The first schematic is a top view of the geometry used in the Couette SANS measurements. The bottom schematic is a side view of the geometry used in the NSSANS measurements with the Poiseuille cell. The hatched areas in both cases represent the liquid sample.

the reflection interface, whereas in SANS it is customary to define the coordinate system with respect to the detector with x and y defining the plane of the detector. In order to maintain some sort of consistency throughout this paper, particularly with respect to the hybrid geometry of the near-surface SANS, we define our Cartesian reference frame with respect to the SANS 2D detector with x horizontal, z vertical and y normal to the detector. The 1D reflectometry detector is defined to be in the z direction.

SANS/NSSANS

The Couette SANS measurements were performed at the CHRNS 30 m SANS spectrometer on the NG3 beam line at the National Institute of Standards and Technology (NIST).[17] Two geometries were used, one at a sample to detector distance (SDD) of 10 m and the other at an SDD of 5 m, both using an incident neutron wavelength of 0.5 nm ($\Delta\lambda/\lambda = 15\%$), yielding Q ranges of $0.05 < Q < 0.5/\text{nm}^{-1}$ and $0.1 < Q < 0.9/\text{nm}^{-1}$, respectively. The NSSANS measurements were performed on the W. C. Koehler 30 m SANS facility at the HFIR reactor at the Oak Ridge National Laboratory.[18] The SDD was 10 m and the incident neutron wavelength was 0.475 nm ($\Delta\lambda/\lambda = 5\%$). The effective

Q range was $-0.37 < Q_x/\mathrm{nm}^{-1} < +0.43$ and $0.113 < Q_z/\mathrm{nm}^{-1} < 0.4$ where Q was limited in the z direction by the sample horizon and critical angle. Collimation was provided by a 10 mm source slit 6.5 m upstream from the sample, and an effective sample slit of 8 mm in the horizontal direction, obtained from a circular aperture directly in front of the sample, and 0.5 mm in the vertical direction, the acceptance of the cell itself. The SANS data were corrected for various background contributions and detector sensitivity and placed on an absolute scale in the usual fashion.[17–19] Corrections for the NSSANS are rather more complex, having to account for volume effects and refraction, and are detailed elsewhere.[20] We note here only that the refraction correction, accounting for the incident beam bending away from the surface normal as it crosses the quartz solution interface and the scattered beam bending towards the surface normal as it crosses the interface and exits the solution, makes the apparent Q_s normal to the surface (Q_z) larger than the real, in-solution, Q_s'.

Couette cell

The cell is constructed of two concentric cylindrical pieces of quartz; the micellar solutions fill the gap between the outer rotating cylinder and the inner stationary cylinder. Thermostatting fluid (25 ± 0.5 °C) circulates through the inner cylinder. Fig. 1 shows the scattering geometry used in our experiment. As the outer cylinder rotates, the solutions are subjected to a laminar flow v_x along the tangent to the cylindrical surface, and the resulting shear gradient $\dot{\gamma} = \partial v_x/\partial y$ is along the direction normal to the cylindrical surface.

Poiseuille cell

A special cell was designed for the NR.[21] For this application the sample must pass through a relatively large area where the interface is perfectly flat and the flow well defined. Planar Couette flow was not deemed feasible and the final design uses Poiseuille flow instead. In order to achieve this, the solutions are pumped through a 1 mm deep trough which is covered by a slab of single crystal quartz polished flat to ⩽8 Å roughness. The trough is 100 mm long and 50 mm wide, providing a significant planar area with lamellar flow (see Fig. 1). The flow profile in Couette flow is different from that in Poiseuille flow.[22] However, in this highly non-Newtonian, viscoelastic system, we expect the high shear-gradient region next to the surface to be similar, and the bulk region of the Poiseuille flow is never sampled in our experiments. Thus we feel that, to a first approximation, the differences can be ignored in this study. The details of the cell are described elsewhere.[21]

Results and Discussion

Fig. 2 shows logarithmic grayscale maps of reflectivity data sets for our 20×10^{-3} M solution of 70/30 CTA3,5ClBz/Br^- in D_2O for neutron contrast, with and without shear ($\langle v \rangle \approx 4$ cm s^{-1} and $\langle v \rangle = 0$ in the Poiseuille cell, respectively). The vertical angular scale has been converted to Q_R, the scattering vector for specular reflection and the horizontal scale has been converted to $Q_Z - Q_R$. The specularly reflected beam signal is clearly apparent in these data sets along $Q_Z - Q_R = 0$. The data points have been normalized for counting time and sample acceptance (proportional to Q and therefore Q_R) above the position of the sample horizon extrapolated onto the detector, $Q_R > 0$. The position where the unscattered incident beam would fall on the detector is marked in the lower left corner of the data sets ($Q_Z = 0$).

Obviously the shear-on data show much stronger off-specular scattering than the shear-off data, the most prominent feature being a sweep of scattering running at

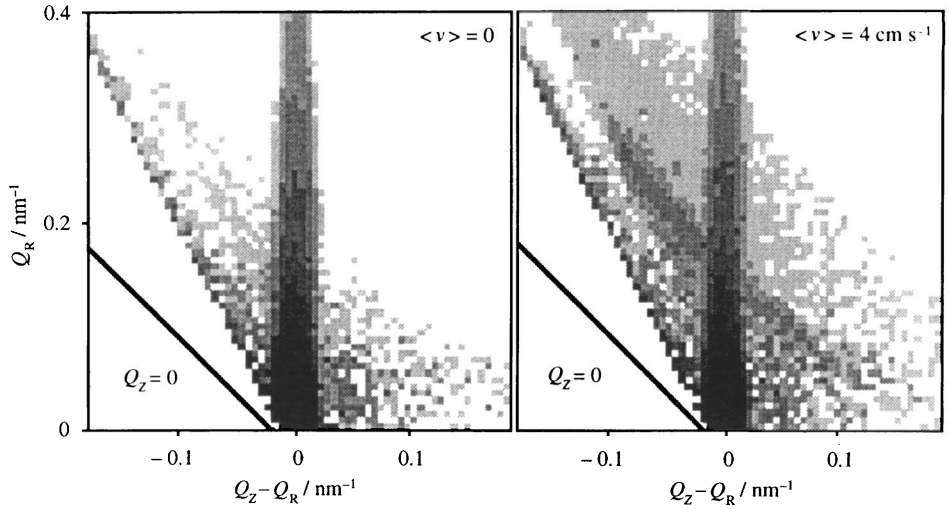

Fig. 2 Grayscale maps of the intensity for the reflectivity measurements from a sample of 20×10^{-3} M 70% CTA3,5ClBz/30% CTAB with the shear off ($\langle v \rangle = 0$) and on ($\langle v \rangle \approx 4$ cm s^{-1}). The main feature, a vertical swath of intensity at constant $Q_z - Q_R$, is the reflected beam. The position of the direct beam is marked by a line at $Q_z = 0$. In the shear-on case a second sweep of intensity, at a constant Qz, roughly parallel to the direct beam line is due to scattering from within the solution.

roughly constant angle to the direct incident beam and crossing the reflected beam diagonally at $Q_R = 0.18$ nm^{-1}. As will be seen shortly, this increased off-specular signal is due to small-angle scattering of the beam transmitted into the solution by shear-induced ordering in the micellar solution as it flows past the quartz surface of the cell. After correcting for refraction, that scattered signal is at $Q'_z = 0.16$ nm^{-1}. For the purposes of a specular neutron reflection measurement the off-specular signal is a variable incoherent background and some care must be taken in subtracting it from the true specular signal. In the present case the value of this signal in the region of the reflection signal ($Q_Z - Q_R = 0$) was obtained by extrapolating from values away from the specular, applying the appropriate corrections for effective sample volume and refraction upon entering and exiting the solution.[20]

The specular reflection coefficient for neutrons is an optical transform in the derivative of the scattering length density profile along the normal to the reflecting interface. At high specular scattering vectors Q_R and low reflectivities this transform may be given by the Rayleigh approximation:[23,24]

$$R(Q_R) \approx \frac{16\pi^2}{Q_R^4} \left| \int_{-\infty}^{+\infty} \frac{d\beta}{dz} \exp(-iQ_R z)\, dz \right|^2 \quad (1)$$

where β is the scattering length density in the medium. $R(Q_R)$ is normalized so that $R(Q_R) = 1$ for $Q_R < Q_c$.

Fig. 3 shows the specular reflection signal for the surfactant solution data sets presented above over the full Q_R range measured with shear-off and shear-on, compared to the reflection signal from a quartz slab on D_2O. The large excess signal at high Q_R in both surfactant data sets may be interpreted as an interference fringe arising from a thin layer adsorbed on the quartz surface. This fringe can be fit by the reflectivity of a 2.5 ± 0.5 nm thick layer of surfactant adsorbed onto the quartz. Since the diameter of the rod-like micelles is well determined and is 4.6 ± 0.6 nm[25] and the radius therefore 2.3 ± 0.3 nm, it is clear that the adsorbed layer is not made up of full worm-like micelles

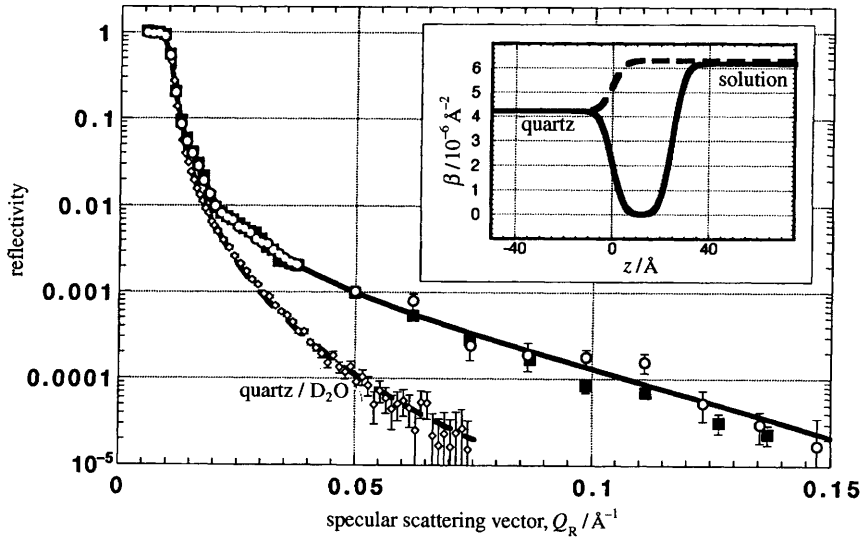

Fig. 3 Reflectivity curves for the same sample as in Fig. 2. (○) shear off and (■) shear on. (◇) Reflectivity from the quartz/pure D_2O interface and are shown for reference. (——) is a fit to both the shear-on and shear-off data which gives the scattering length density (β) profile shown by the solid line in the inset; (— —) is a fit to the D_2O data with the β profile of the dashed line in the inset.

as has recently been reported for C_{14}TAB on mica or even the spherical micelles reported for the same system on silica.[26] The resolution is insufficient, however, to distinguish between a single monolayer (or hemispherical micelles) and an interdigitated bilayer as has been suggested for CTAB on quartz[27] and which might be expected from the hydrophilic nature of quartz. Whatever the exact structure, there is apparently no shear effect on this adsorbed layer.

The question remains as to the origin of the one obvious shear-dependent feature, the relatively strong scattering (refraction corrected) signal at $Q'_z = 0.16$ nm^{-1}. As with any charged colloidal suspension (without supporting electrolyte), bulk SANS from this solution at rest gives rise to an interaction ring of scattering[28] which is at that Q [Plate 1(a)]. Under Couette shear [Plate 1(b)], the rods align with the flow as expected[29] and the ring of scattering collapses into two scattering peaks in a Q_s direction perpendicular to that flow. The fact that the rods align and that the scattering now contains two peaks in place of the ring does not imply, of itself, anything other than 3D liquid-ordering collapsing into 2D liquid-ordering. Further, while the peak height in the sheared solution is stronger than that of the isotropic ring of scattering in the unsheared case, it is not sufficiently so to account for the total absence of a scattering feature in the shear off NR data.

Besides the two main peaks in our Couette data, there is a smaller set of peaks at a slightly higher Q, indicating that in fact more is happening than the classical 2D liquid alignment of the rods. The position of these secondary peaks, which have no corresponding ring visible in the unsheared data, is at *ca.* 1.8 times the Q value of the primary peaks. 1.8 is close enough to $\sqrt{3}$ to make it tempting to interpret this as rods aligning hexagonally, as has been done for the double-tail cationic surfactant system of *N*-hexadecyloctyldimethylammonium bromide (C_8C_{16}DAB).[30] One must be very cautious of over interpreting limited data. However, if the second peak is due to hexagonal ordering, that ordering would be in the plane perpendicular to the flow. Ideally, one should then attempt to measure the scattering with the incident beam parallel to the flow.

Plate 1(a)

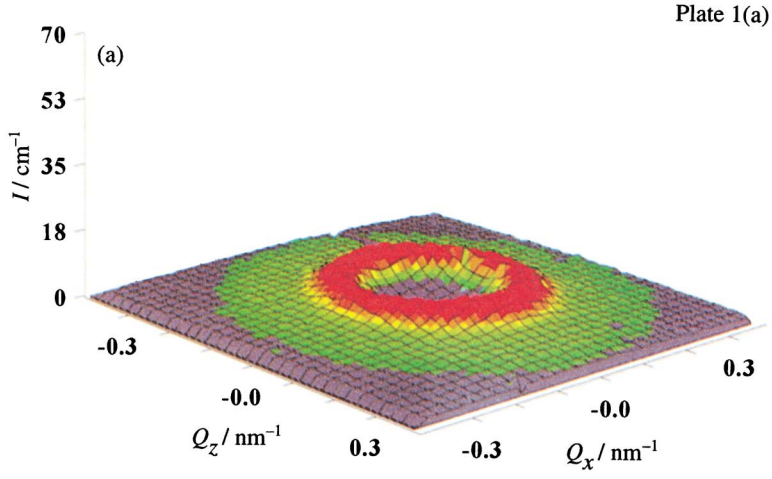

Plate 1(b)

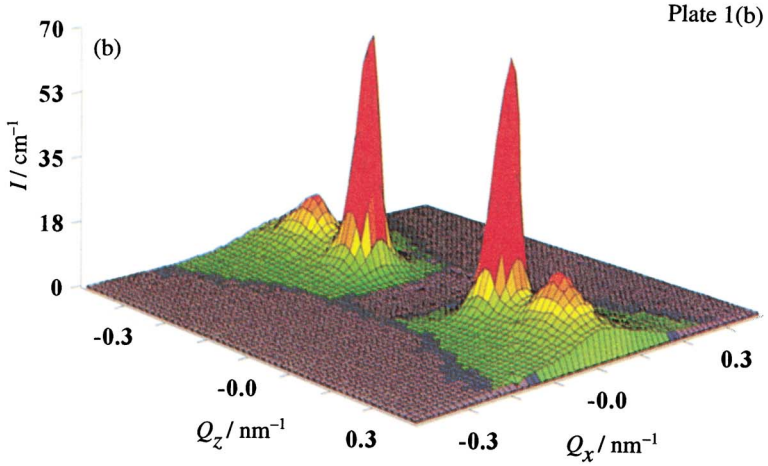

Plate 1 3D SANS surface plots for the system of Fig. 2 using Couette flow. (a) Is the isotropic scattering pattern obtained with the shear off; (b) is the scattering pattern after full alignment in the Couette cell (nominal $\dot{\gamma} = 40$ Hz). Both data sets are on the same scale for comparison.

By using the Poiseuille cell and essentially repeating the reflectometry experiment using a 2D SANS camera as the detector, one can access the two dimensions of interest in verifying the existence of a hexagonal structure. This could technically also be done in the standard Couette cell on SANS, by moving the beam so that it traverses the cell tangentially rather than radially. While this has been done successfully for some polymer systems,[31] there are several benefits to the reflection geometry SANS approach. First, if one is looking for a crystalline-type structure it would be preferable for its axis to remain in the same orientation with respect to the incident beam throughout the probed volume. Assuming that under flow any structures established will have the flow direction as a primary axis, as is the case here, it is important to keep the angle between the flow direction and the incident beam constant. This is achieved in the reflection geometry by definition, while it is not in the Couette geometry (though how much of the scattering comes from the various orientations depends on a number of parameters, some of which are poorly controlled). Secondly, the smeared reflection and the curved surface of the

Couette cell make it extremely difficult to apply the corrections necessary for a quantitative evaluation of the structure formed. Finally, and of most interest to this discussion, the Poiseuille geometry limits the depth from the interface that is probed due to the absorption of neutrons by the sample itself (the macroscopic absorption cross-section, $\Sigma_a \approx 0.9$ cm^{-1}, is more than an order of magnitude greater than the macroscopic scattering cross-section Σ_s of *ca.* 0.05 cm^{-1}). For a neutron to enter the solution at a grazing angle, scatter at small angle and exit the solution back through the liquid/quartz interface, requires it to travel a fair distance in the sample, a distance which increases rapidly with the depth at which the scattering event takes place. The depth to which the SANS 'sees' then is determined by the maximum pathlength in solution which, in turn, is determined by the absorption of the sample at the given wavelength and by the angle of incidence. In our system, that depth is of the order of 30 μm. Thus, we have a tool which is again probing the near-surface structure, albeit over a deeper region than probed by the reflectometry. Furthermore, this geometry will show directly the scattering feature responsible for the NR streak. The disadvantage to this method is that it is rather limited in the Q range attainable because of horizon problems, critical edge limitations and interference from the reflected beam.

In this experiment, as for the NR experiment, the incident neutron beam is parallel to the flow direction. Doing all the corrections, including those for volume and refraction, leads to the 2D patterns for shear-on ($\langle v \rangle \approx 9$ mm s^{-1} through the cell) and shear-off shown in Plate 2. The strongest feature in both data sets is the intense reflected beam. With no shear there is little else visible, not even the isotropic scattering ring discussed earlier. With the shear on, however, a multitude of other spots appear revealing not only the existence of a hexagonal structure in solution, but an oriented, 'single-crystal' hexagonal structure.

Though difficult to view on a single scale, there are nine peaks visible in the data which can be hexagonally indexed as 01, 10, $\bar{1}1$, 02, 11, $\bar{1}2$, 20, 22 and $\bar{2}3$. The $\bar{2}3$ peak is extremely weak, while the relatively strong 10 and $\bar{1}1$ peaks are partially masked by the horizon making both their intensity and their exact position difficult to judge. The angle between the 01 to 11 line and the 01 to 02 line is the same as the angle between the 01 to 02 line and the 01 to $\bar{1}2$ line and is $60 \pm 1°$, while the angles between the $Q = 0$ position and the 11 and 01 peaks and the 01 and $\bar{1}1$ is $30 \pm 1°$. This is, therefore, clear evidence for an undistorted hexagonal lattice.

Besides the spacing of the scattering planes of 39 nm, and therefore the nearest-neighbour separation of 45 nm, there are several other pieces of information that can be extracted from a crystal pattern such as this; $\Delta d/d$ or the fluctuation in the rod spacings; Δr or the amount of lateral motion the rods have around their lattice position (from the Debye–Waller factor); the degree of orientational order (single-crystal *vs.* powder pattern) and the mosaic width of the crystal giving a sense of the length-scale over which the rods behave as rigid objects. Of course, in this case, the amount of sample doing the scattering, 1% of a 0.02 ml volume (8 mm × 100 mm × 30 μm), is quite small and long exposure times are therefore required to obtain statistics sufficient for a reasonably good crystallographic analysis. Obtaining the mosaic width is particularly difficult here since, not only are the scans of relatively short duration, but of the three peaks with reasonable intensity, the 01 is experimentally inaccessible and the problems associated with accurate intensity measurements on the other two, the 10 and $\bar{1}1$, have already been pointed out.

Measuring the radial width of the peaks gives us a $\Delta Q/Q$ value of $29 \pm 5\%$ FWHM leading to a $\Delta d/d$ of 27%. By analysing the relative intensities of the peaks a Δr_z value of 5.9 ± 0.5 nm and a much less well defined Δr_x of 6 ± 2 nm are obtained. The tangential width of the peaks fit to Gaussians is $25 \pm 5°$ FWHM, giving the average orientational order over the depth probed. Finally, the best estimate for the mosaic width, given the experimental difficulties, is of the order of $7.5 \pm 2.5°$, when corrected for the angle

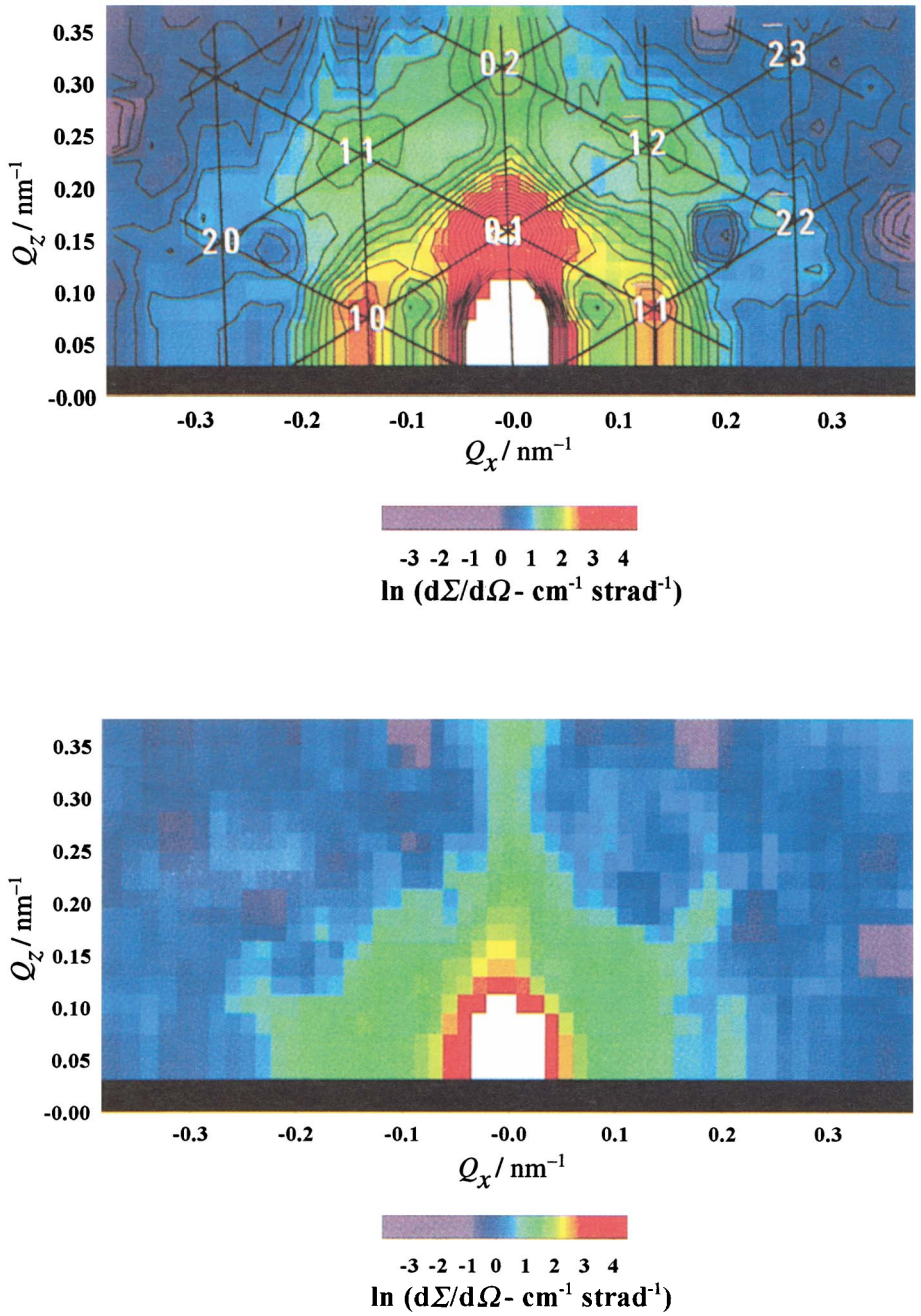

Plate 2 2D NSSANS surface plots for the system of Fig. 2 using Poiseuille flow. The bottom image is with the shear off, while the top image is with the shear on ($\langle v \rangle \sim 9$ mm s^{-1}). Both data sets have been smoothed twice and put on the same log scale for comparison. The white area in both images is the reflected beam. A contour plot and an indexed hexagonal grid have been superimposed on the shear-on image as a visual aid. The incident angle in both cases is 0.26°.

between the correct rocking curve axis and the experimental one [a cos(30) correction]. For reference, a slightly higher concentration of a slightly different CTA3,5ClBz to CTAB ratio, such that the two peaks of interest were not so close to the scattering horizon, was measured at $4.5 \pm 0.4°$.[32]

While this structure behaves as a single crystal in terms of the scattering, albeit a rather poor one by normal solid-crystal standards, it is rather unique and remarkable. The flow-aligned rod-like micelles associated with the lattice positions, and responsible for the scattering, are moving, and there is thus a constant turnover of the rods at each of the lattice positions. Further, the planes responsible for the Q_z diffraction spots being at different depths from the interface are presumably, given the flow profile of the solution, moving at different velocities. Finally, there is the point that these thermodynamically formed objects, are moving in a relatively stable formation, maintaining not only their separation distance of some eight times their diameter, but also the specific direction, with respect to the flow field, to their nearest, freely flowing, neighbour (which, as mentioned above, is constantly being replaced by a different neighbour but at the same relative position with respect to the original micelle).

It is thus clear that the scattering signal in the reflectometry and in the NSSANS are visible only because the isotropic signal collapses not only into a constant (Q_x, Q_z) ring but in fact into six distinct Bragg diffraction spots. However, this crystalline structure is only demonstrated near the surface. While the $\sqrt{3}Q_0$ peak in the bulk Couette data is also consistent with a hexagonal structure, some more care needs to be given to that question which could be rephrased to ask: what happens to the near-surface hexagonal crystal structure as a function of distance from the interface?

Considering the structure found near the surface, and the fact that the system is a solution of rods aligned parallel to the flow, only three possible scenarios for the bulk structure seem viable. First, the crystalline order could be driven entirely by the hydrodynamics and electrostatics of the solution such that the oriented hexagonal structure persists throughout the bulk. Second, the hexagonal structure could still be driven by the hydrodynamics and electrostatics, with only the orientational constraint coming from the anisotropy imposed on the system by the proximity of the surface. Finally, the proximity of the surface could drive the hexagonal structure directly, in which case the most likely structure for the bulk would be a 2D liquid.

The first possibility can easily be disproven. In the Couette geometry, the beam is parallel to the shear gradient and structures in the plane perpendicular to that gradient are probed. When viewing a hexagonal crystal perpendicularly to the c axis (the rod direction), there are two different sets of planes causing Bragg diffraction with one giving rise to scattering at Q_0 and the other at $\sqrt{3}Q_0$. Which planes are visible depends on the viewing angle. The diagram in Fig. 4 makes it clear that, in the Couette geometry, only the $\sqrt{3}Q_0$ peak would be visible. As mentioned earlier with reference to Plate 1, by far the most prominent feature in the Couette data is the peak at Q_0. Thus, either the first peak is mainly a liquid-structure-factor peak from the bulk, with the second peak coming from the near-surface hexagonal structure, or the bulk structure is a non-oriented hexagonal or 2D powder. If the first is the case, it is difficult to conceive of there not being some transition region in which the structure is an unoriented hexagonal so that both peaks would probably contain some contribution from such a structure anyway. In the second case, since the measurement is an average through the entire sample, there must be some contribution to the $\sqrt{3}Q_0$ peak from the oriented crystal near the surface. In fact, assuming a 2D powder structure in the bulk, the $\sqrt{3}Q_0$ peak should be at least 3% stronger than the Q_0 peak, since the gap is 1 mm and the structure is known to be oriented to a depth of at least 30 μm (in the Couette geometry it is not clear how the stationary interface compares to the Poiseuille interface).

In order to differentiate between these two possibilities, the easiest test is to assume the simplest case, that the bulk structure is a 2D powder, and verify that the data are

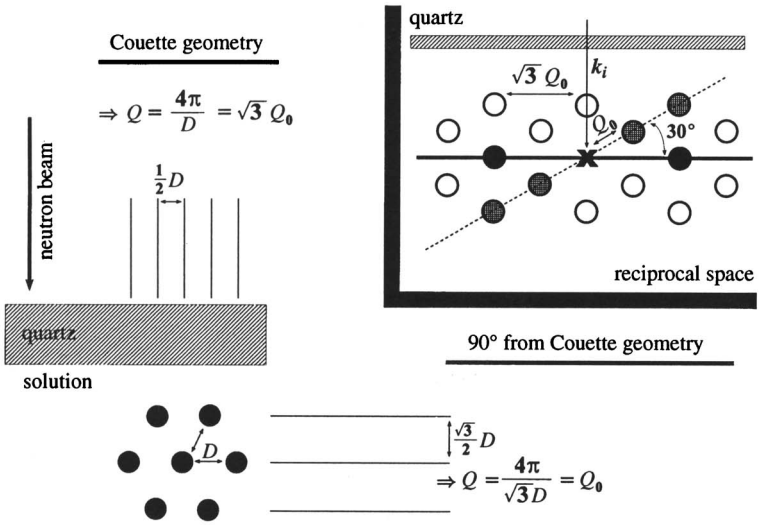

Fig. 4 Diagram showing the spacing of the scattering planes available in the Couette geometry and for the neutron beam at 90° from that in the Couette geometry assuming the crystal orientation found by NSSANS. This clearly shows that the spacing of the planes doing the scattering in the Couette geometry is smaller (and its Q bigger) than if the neutron beam were at 30° or 90° from its actual direction. The inset gives the same information in reciprocal space. The solid line in the inset represents the detector plane (or Ewald 'plane') and the solid spheres are those spots which intersect that plane and are therefore the only visible ones. The dashed line is the effective detector plane assuming the crystal were tilted by 30°, and the cross-hatched spheres are those that would be visible in that case.

consistent with that model. For this, a knowledge of how the intensity varies with Q is needed. All the Bragg spots in a single crystal will have the same base intensity attenuated by the form factor of the particle (a Q-dependent term) and the Debye–Waller factor discussed in connection with the oriented hexagonal structure. In the 2D powder, every possible crystal orientation is represented by some micro-crystallite in the powder such that all the spots at a constant $Q[Q = (\sqrt{Q_x^2 + Q_y^2})]$ appear in a single ring of scattering. In the Couette geometry, the beam is parallel to the plane of that ring and the detector is therefore perpendicular to it, so that the reciprocal space ring of intensity only intersects the detector in two spots. Because these spots actually come from a ring, there are two more corrections which must be made:[33] a multiplicity correction and a Lorentz correction. The multiplicity factor, m, accounts for rings containing different numbers of Bragg peaks ($m = 1$ for rings containing 6 Bragg peaks and 2 for those containing 12) and the Lorentz factor for the fact that rings at higher Q 'spread' their intensity over a larger reciprocal space ring (and therefore the average intensity per unit length of that reciprocal ring is inversely proportional to its circumference and therefore its Q). Finally, each peak has some width which is modelled as a Gaussian of full-width at half-maximum (FWHM) σ_i. σ_i itself is Q dependent and is normalized here to the width of the first peak such that $\sigma_i = \sigma Q_i/Q_0$, where Q_0 is the Q position of the first peak and Q_i is the Q position of the ith peak. The scattered intensity $I_s(Q)$ can then be written:

$$I_s(Q) = I_n P(Q) \sum_i m \exp(-Q_i^2 \Delta r^2) \exp[-(Q - Q_i)^2/2\sigma_i^2] + B_{inc} \qquad (2)$$

where the sum is over all Bragg rings, I_n is a scaling factor, $P(Q)$ is the form factor, $1/Q$ is the Lorentz correction and B_{inc} is the flat incoherent background. The form factor is known and is independent of the data, as is the multiplicity factor. The incoherent background can be calculated from tabulated values and knowledge of the concentration of

each element present in the system. The Q position of all the peaks are determined by the first one and go as Q_0, $\sqrt{3}Q_0$, $2Q_0$, $\sqrt{7}Q_0$, $3Q_0$ *etc.* Since the data go out to a $Q = 0.7$ nm^{-1} the first 10 rings were used [up to $\sqrt{(21)}\,Q_0$]. There are thus only four variable parameters in this equation: Q_0 the position of the first peak; I_n a scaling factor; σ the width of the first peak and Δr from the Debye–Waller factor. Furthermore, the first three parameters are more or less fixed by the first peak. The fourth variable, Δr, could be fixed as well by the value from the NSSANS data. However, it is possible that the surface which causes the crystal to orient, also restricts the amount of motion the rods have, thereby making Δr smaller near the surface. It is therefore left as the only variable with which to fit the rest of the curve. This is a fairly rigorous test of the model.

Fig. 5 shows the results from three different fits. The important point to be made is that, given that the first three parameters are set by the first peak, with $Q_0 = 0.164$ nm^{-1} and $\sigma = 0.025$ nm^{-1}, the second peak, including its hump due to the $2Q_0$ peak, can be fit quite well with a Δr of 4.1 nm (I_n is 1.0 cm^{-1} and is determined by the first peak and Δr). However, the tail of the curve (*i.e.* the last six peaks) is completely missed. Since this measurement is an average of the surface and bulk structures, some of the $\sqrt{3}Q_0$ peak should be due to the near-surface crystal (which contributes nothing to any of the other peaks except the $2\sqrt{3}Q_0$ peak) and therefore the calculated curve should be less intense at that point than the data. That would be consistent with the small value obtained for Δr compared to that from the NSSANS, but, unfortunately, it makes the discrepancy in the tail region even worse. In fact the entire tail region cannot be fit at all unless the requirement that the magnitude of the intensity be set by the first peak be abandoned. Relaxing that requirement gives a marginally reasonable fit for the entire tail region (peaks $>2Q_0$), while giving a primary peak which is far too weak. Not only is that physically unreasonable given the model, so is the Δr of only 2 nm required to achieve that fit which is far less than measured in the near-surface crystal. Finally, relaxing the requirement that σ be determined by the first peak gives a near perfect fit in the tail for $\sigma = 0.1$ nm^{-1} and $\Delta r = 1$ nm, while leaving no peak in the calculated curve whatsoever. The unreasonableness of the fit is even greater than previously for the same reasons. Thus, despite the 'single-crystal' behaviour near the surface, the weight of the evidence for this system is against the bulk solution hexagonal structure postulated for the C_8C_{16}DAB system.[30] This would indicate that the surface is the driving force for the

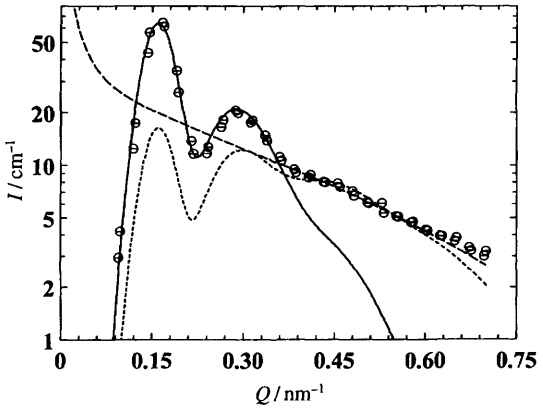

Fig. 5 Intensity as a function of Q_y at constant $Q_x = 0$ for the data in Fig. 4(b). The solid line is a fit to the first two peaks (effectively the first three Gaussians) with $Q_0 = 0.164$ nm^{-1}, $I_n = 1$ cm^{-1}, $\sigma = 0.25$ nm^{-1} and $\Delta r = 4.1$ nm (see text for details). (— —) Represents a fit with Q_0 and σ set the same as previously and $I_n = 3$ cm^{-1} and $\Delta r = 2$ nm; (—·—) is for the same Q_0 but $I_n = 0.54$ cm^{-1}, $\sigma = 0.1$ nm^{-1} and $\Delta r = 1$ nm.

hexagonal ordering rather than just a wall condition which forces the hexagon to become oriented in its proximity.

The picture that emerges then, is of a near-surface oriented hexagonal crystal going eventually to no crystalline order in the bulk. The most realistic model for the metamorphosis would be a gradual evolution from very ordered and oriented to ordered without orientation to no order, rather than a sudden mutation from crystalline to non-crystalline. This idea is supported by the existence of a distinct shoulder on the $\sqrt{3}Q_0$ peak at $2Q_0$. The intensity necessary for the $2Q_0$ peak to be so pronounced implies a Bragg reflection rather than a liquid peak. Such a reflection would be impossible as noted earlier without the crystal rotating 30° (and thus giving rise to a 2D powder). Further, there is some evidence in the NR data for some very weak secondary fringes at low Q_R. While work continues in this area, the preliminary suggestion is that there may be a few low contrast layers strongly correlated with the surface. One possible interpretation is that the first plane of the hexagon is pinned by the surface and therefore very well correlated with it, though it appears that hexagon may also be somewhat modified by the adjacent surface.

Conclusions

We have demonstrated that, by using a variety of geometries and techniques, it is possible to obtain a fairly comprehensive picture of structures formed under flow in the near-surface region, as well as in the bulk. In the case of our system of viscoelastic, rod-containing, micellar solutions, we find that a single layer of surfactant is adsorbed onto the quartz surface and is unaffected by the application of shear. Under a flow field the rods in the bulk appear to orient along the flow, exhibiting a 2D liquid-like ordering. In the near-surface region, however, the physical constraint imposed by the interface, as well as possible electrostatic interactions between the rods and the surface layer, force the rods to align in an ordered hexagonal pattern with the *c* axis along the flow direction. The hexagonal structure decays with distance from the surface by losing orientational order, going from single crystal like behaviour to 2D powder behaviour, before going to the completely liquid-like ordering found in the bulk. Note that not all systems of rod-like micelles form this near-surface hexagonal structure. For example, no hexagonal structure has yet been seen in a 20×10^{-3} M solution of pure CTA3,5ClBz at the flow rates presently attainable and the depths over which we are averaging. Thus, by making a systematic study of appropriately chosen rod-containing micellar solutions, it should be possible to develop a theoretical framework for understanding the interactions which lead to this remarkable behaviour.

This work was supported by the US Department of Energy under Contract DE-AC05-96OR22464 with Lockheed Martin Energy Research, and by the National Science Foundation, CHE-9008589. Some of the SANS measurements were performed on the NIST NG3 instrument, which is supported by NSF under agreement DMR9122444. Identification of certain equipment or materials does not imply recommendation by NIST. The Oak Ridge Institute for Science and Education provided financial support for P. D. B.

References

1 F. Quirion and L. J. Magid, *J. Phys. Chem.*, 1986, **90**, 5435.
2 P. Debye and E. W. Anacker, *J. Phys. Colloid Chem.*, 1951, **55**, 644.
3 S. J. Candau, E. Hirsch, R. Zana and M. Adam, *J. Colloid Interface Sci.*, 1988, **122**, 430.
4 L. S. C. Wan, *J. Pharm. Sci.*, 1966, **55**, 1395.
5 L. S. C. Wan, *J. Pharm. Sci.*, 1967, **56**, 743.
6 R. M. Bain and A. J. Hyde, *Faraday Symp. Chem. Soc.*, 1971, **5**, 145.

7 S. Gravsholt, *J. Colloid Interface Sci.*, 1976, **57**, 575.
8 M. T. Carver, Ph.D. dissertation, The University of Tennessee, Knoxville, Tennessee, 1986.
9 M. Carver, T. L. Smith, J. C. Gee, A. Delichere, E. Caponetti and L. J. Magid, *Langmuir*, 1996, **12**, 691.
10 P. D. Butler, L. J. Magid, W. A. Hamilton, J. B. Hayter, B. Hammouda and P. J. Kreke, *J. Phys. Chem.*, 1996, **100**, 442.
11 J. Penfold and R. K. Thomas, *J. Phys.: Condens. Matter*, 1990, **2**, 1369.
12 T. P. Russell, *Mater. Sci. Rep.*, 1990, **5**, 171.
13 J. R. Lu, E. A. Simister, R. K. Thomas and J. Penfold, *J. Phys. Chem.*, 1993, **97**, 6024.
14 E. Staples, L. Thompson, I. Tucker, J. Penfold, R. K. Thomas and J. R. Lu, *Langmuir*, 1993, **9**, 1651.
15 W. A. Hamilton, J. B. Hayter and G. S. Smith, *J. Neutron Res.*, 1994, **2**, 1.
16 M. Yethiraj and J. A. Fernandez-Baca, in *Neutron Scattering in Materials Science II*, ed. D. Neumann, T. Russel and B. Wuensch; Materials Research Society, Pittsburgh, Pennsylvania, 1995, p. 59.
17 B. Hammouda, S. Kruger and C. Glinka, *NIST J. Res.*, 1993, **98**, 31.
18 W. C. Koehler, *Physica B*, 1986, **137**, 320.
19 G. D. Wignall and F. S. Bates, *J. Appl. Crystallogr* 1986 , **20**, 28.
20 W. A. Hamilton, P. D. Butler, John B. Hayter, L. J. Magid and P. J. Kreke, *Physica B*, 1996, in the press.
21 S. M. Baker, G. Smith, R. Pynn, P. Butler, J. B. Hayter, W. A. Hamilton and L. Magid, *Rev. Sci. Instrum.*, 1994, **65**, 412.
22 J. B. Hunter, *Foundations of Colloid Science*, Oxford University Press, Oxford, 1989, Vol. II, Ch. 18.
23 J. Lekner, in *Theory of Reflection of Electromagnetic and Particle Waves*, Martinus Nijhoff, Dordrecht, 1987, Appendix A-5.
24 J. Lekner, *Physica B*, 1991, **173**, 99.
25 P. D. Butler, L. J. Magid and J. B. Hayter, in *Structure and Flow in Surfactant Solutions*, ed. C. A. Herb and R. K. Prud'homme; American Chemical Society, Washington, DC, 1994, p. 250.
26 M. Srinivas and H. E. Gaub, *Science*, 1995, **270**, 1480.
27 D. C. McDermott, J. McCarney, R. K. Thomas and A. R. Rennie, *J. Colloid Interface Sci.*, 1994, **162**, 304.
28 SANS from this solution at rest has also been measured in the usual fashion (static SANS). Those results are as yet unpublished.
29 J. B. Hayter and J. Penfold, *J. Phys. Chem.*, 1984, **88**, 4589.
30 J. Kalus, H. Hoffmann, S-H. Chen and P. Lindner, *J. Phys. Chem.*, 1989, **93**, 4267.
31 C. L. Jackson, F. A. Morrison, A. I. Nakatani, J. W. Mays, M. Muthukumar, K. A. Barnes and C. C. Han, in *Flow Induced Structures in Polymers*, ed. A. I. Nakatani and M. D. Dadmun; American Chemical Society, Washington, DC, 1995, p. 233.
32 W. A. Hamilton, P. D. Butler, S. M. Baker, G. S. Smith, J. B. Hayter, L. J. Magid and R. Pynn, *Phys. Rev. Lett.*, 1994, **72**, 2219.
33 Jerold M. Schultz, *Diffraction for Materials Scientists*, Prentice Hall, New Jersey, 1982.

Paper 6/03735F; *Received* 29*th May*, 1996